ACS Catalysis

Research Article

pubs.acs.org/acscatalysis

Titania-Decorated Silicon Carbide-Containing Cobalt Catalyst for Fischer–Tropsch Synthesis

Yuefeng Liu,*[,†] Benoit de Tymowski,[†] Fabrice Vigneron,[†] Ileana Florea,[‡] Ovidiu Ersen,[‡] Christian Meny,[‡] Patrick Nguyen,[§] Charlotte Pham,[§] Francis Luck,[⊥] and Cuong Pham-Huu*[,†]

[†]Laboratoire des Matériaux, Surfaces et Procédés pour la Catalyse (LMSPC), UMR 7515, CNRS-Université de Strasbourg (UdS), 25, rue Becquerel, 67087 Strasbourg Cedex 08, France

[‡]Institut de Physique et Chimie des Matériaux de Strasbourg (IPCMS), UMR 7504, CNRS-Université de Strasbourg (UdS), 23, rue du Loess, 67034 Strasbourg Cedex 02, France

[§]SICAT/ACM Technical Center, Industriestrasse 1, D-77731 Willstätt, Germany

[⊥]Total, Direction Générale-Direction Scientifique, 24 cours Michelet, F-92069 Paris La Défense Cedex, France

Supporting Information

ABSTRACT: The metal–support interactions of titanium dioxide decorated silicon carbide (β-SiC)-supported cobalt catalyst for Fischer–Tropsch synthesis (FTS) were explored by a combination of energy-filtered transmission electron microscopy (EFTEM), ^{59}Co zero-field nuclear magnetic resonance (^{59}Co NMR), and other conventional characterization techniques. From the 2D elemental maps deduced by 2D EFTEM and ^{59}Co NMR analyses, it can be concluded that the nanoscale introduction of the TiO_2 into the β-SiC matrix significantly enhances the formation of small and medium-sized cobalt particles. The results revealed that the proper metal–support interaction between cobalt nanoparticles and TiO_2 led to the formation of smaller cobalt particles (<15 nm), which possess a large fraction of surface atoms and, thus, significantly contribute to the great enhancement of conversion and the reaction rate. The cobalt time yield of the catalyst after modification increased to 7.5×10^{-5} mol_{CO} g_{Co}^{-1} s^{-1} at 230 °C, whereas the C_{5+} selectivity maintained a high level (>90%). In addition, the adequate meso- and macro-pores of the SiC-based support facilitated intimate contact between the reactants and active sites and also accelerated the evacuation of the intermediate products. It was also worth noting that a superior and stable FTS specific rate of 0.56 $g_{C_{5+}}$ $g_{catalyst}^{-1}$ h^{-1} together with high C_{5+} selectivity of 91% were obtained at common industrial content of 30 wt % cobalt.

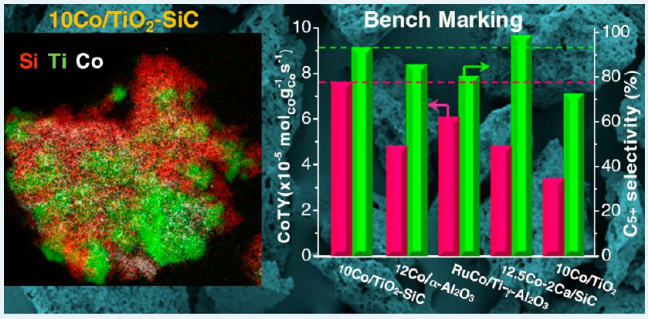

KEYWORDS: *metal–support interaction, Fischer–Tropsch synthesis, silicon carbide, cobalt, titanium oxide, energy-filtered TEM, ^{59}Co NMR, catalysis*

1. INTRODUCTION

Fischer–Tropsch synthesis (FTS) is a key technology in the more global gas-to-liquids (GTL) process, which allows the transformation of synthesis gas ($2H_2$ + CO), issued from natural gas reforming into liquid hydrocarbons, followed by hydrocracking of the heavy fraction into useful compounds, such as naphtha, diesel, lubricants, and others.[1−6] The most employed active phase for the low-temperature FTS process is supported cobalt, either pure or doped with trace amounts of noble metal to enhance the reduction of the active phase and to improve the dispersion of metal particles.[7−11] Cobalt presents several advantages, such as high stability, high activity for liquid hydrocarbons formation and low selectivity toward oxygenated products, resistance to oxidation, low water-gas shift (WGS) tendency, and acceptable price for industrial development. However, the high activity of the cobalt phase also leads to an extremely high sensitivity of the catalyst selectivity to the reaction temperature. Cobalt active phase is typically employed in a supported form for the FTS process. The support should display a relatively high specific surface area to achieve a high dispersion of the metal particles, good mechanical and hydrothermal resistance, and a medium level of metal–support interaction to allow complete reduction of the active phase and to prevent sintering of the cobalt. The most employed supports for the FTS are alumina; silica; titania; and carbon-based materials, such as activated carbon, carbon nanotubes, and nanofibers.[12−19] Among these supports, alumina, either pure or promoted, is the most employed as a support for commercial catalysts. However, on traditional supports such as alumina and silica, it is difficult to reduce small particles of metal oxide

Received: November 11, 2012
Revised: January 17, 2013
Published: January 22, 2013

precursor because of the presence of high metal−support interactions that prevent the complete reduction of the active phase oxide precursor at moderate temperatures.[20−22] In addition, the low thermal conductivity of alumina could lead to the formation of local hot spots during FTS, which compromise the selectivity of the reaction and the plant safety, especially at high CO conversion. Wang et al.[23] reported that the heat release by the FTS cannot be properly evacuated to the entire body of the alumina support and, thus, leads to the formation of hot spots on the catalyst surface, which favors formation of light products. It is therefore of interest to develop new supports with improved thermal conductivity to reduce as much as possible the temperature gradient within the catalyst bed. Supports with high chemical inertness also show advantages for the recovery of the active phase at the end-life of the catalyst, taking into account the toxicity of cobalt and its relatively high amount in the FTS plant. Such new supports should also be inexpensive and readily available in various shapes to reduce the costs linked with the reactor modifications.

Recently, silicon carbide (β-SiC) with medium specific surface area (20−40 $m^2\ g^{-1}$) has been reported as an efficient support for FTS allowing working at high CO conversion along with a high C_{5+} selectivity, as well as for the FTO (syngas to olefins) reaction with high selectivity toward light olefins.[24−29] Silicon carbide possesses all the physical properties required for being used as a catalyst support;[30−32] namely, high mechanical strength, high thermal conductivity (which allows a rapid homogenization of the temperature within the catalyst bed), high oxidative resistance, and chemical inertness (which facilitate the recovery of the active phase and the support for subsequence reuse[24]). It is also worth noting that the pore network of SiC consists of mainly meso- and macropores, which significantly enhances mass transfer during FTS and prevents the formation of concentration gradients between hydrogen and carbon monoxide, which leads to the formation of light products.

A catalyst containing 30 wt % Co/1.0 wt % Ru support on high surface area and hierarchical macromesoporous structure γ-Al_2O_3 nanofibers has been reported by Martínez et al.[33] to evidence the diffusion and dispersion effects during FTS comparable to commercial alumina (Sasol). The benefits of using the macromesoporous nanofibrous support (high Co^0 dispersion and fast CO transport rate through the liquid phase filling the pores) are evidenced at high metal loadings (30 wt % Co), at which the nanofibrous catalyst displays the highest specific activity and productivity to diesel products. Indeed, during FTS, the catalyst pores are mostly filled with liquid waxes, and thus, both gaseous reactants and FTS products have to diffuse through a liquid layer. Such a gas−liquid diffusion layer causes more severe concentration gradients for CO than for H_2 because of the higher diffusivity of the latter. The difference in terms of the diffusivity of the reactants leads to the formation of a high local concentration of H_2 versus CO and, as a consequence, a higher selectivity toward light products formation. It was suggested that a higher diffusion rate of hydrogen inside the pores filled up with liquid products compared to that of carbon monoxide entailed an increase in the local H_2/CO ratio in the catalyst pores and, thus, a shift toward the formation of lighter hydrocarbons, especially methane.[34,35]

The β-SiC support also presents a low metal−support interaction, which allows an easy reduction of the deposited metal particles at moderate reduction temperature.[24,25] However, the low metal−support interaction also prevents the high and homogeneous dispersion of the metal nanoparticles on the SiC-based support, leading to a relatively large metal particle size (30−40 nm), which is higher than that desired for the optimum operation of the FTS process (6−20 nm).[16,36] It is thus of interest to develop a new SiC-based support for such a highly demanding catalytic process with a higher surface area and a stronger metal−support interaction to improve active phase dispersion and also to prevent excessive metal particle size growth by hydrothermal sintering during the course of the reaction.

In the general framework related to the study of multiphase nanomaterials synthesized in a powder form, a key challenge is the determination of the relative spatial distribution of the components, especially at the surface of the grains. For instance, for the catalytic supports made of several components, one of the crucial parameters is their relative amount at the surface, to be correlated to the distribution of the active phase nanoparticles. In that regard, the most appropriate technique that can provide elemental maps on a field of view of a few hundred nanometers is energy-filtered transmission electron microscopy (EFTEM) technique.[37,38]

The aim of the present study is to report on the development of a new hybrid support, titanium dioxide-decorated silicon carbide with improved metal−support interactions, and its use in the Fischer−Tropsch synthesis. Titanium dioxide exhibits a high metal−support interaction with the cobalt active phase precursor, which leads to a higher dispersion of the cobalt particles compared with those deposited on the SiC surface. These small cobalt particles (<15 nm) significantly improve the performance of the FTS catalyst without sacrificing the high selectivity toward liquid hydrocarbons already observed on such oxide supports. The correlation between catalyst structure and catalytic performance was supported by advanced characterization techniques, such as ^{59}Co zero-field nuclear magnetic resonance (^{59}Co NMR) and EFTEM along with more conventional characterization techniques (high-resolution TEM, temperature-programmed reduction (TPR), XRD, etc.). The potential industrial development of this catalyst will also be evaluated with a long-term FTS test. Finally, the catalytic performance of the Co/TiO_2−SiC catalyst will be benchmarked with those of different FTS catalysts reported in the literature.

2. EXPERIMENTAL SECTION

2.1. TiO_2-Decorated SiC Support Synthesis. β-SiC was synthesized via a gas−solid reaction between SiO vapor and dispersed solid carbon. The detailed synthesis of the SiC-based materials was summarized in a recent review.[39] The titania-decorated β-SiC was synthesized by mixing microsized silicon powder and TiO_2 nanoparticles with a carbon-containing resin. The paste was further processed into various shapes, such as extrudates, grains, beads, etc. Examples of SiC with different sizes and shapes are presented in Figure 1. The carbidization process was carried out under flowing argon at temperatures around 1350 °C over 1 h. The argon flow allows removal of the CO formed during the reaction from the reactor and, thus, shifting of the reaction toward the formation of SiC. The resulting composite contains SiC intimately mixed with TiC. The TiC-to-TiO_2 transformation was carried out by treating the composite at 550 °C in air for 2 h. The details of the synthesis can be found in ref 39.

dx.doi.org/10.1021/cs300729p | ACS Catal. 2013, 3, 393−404

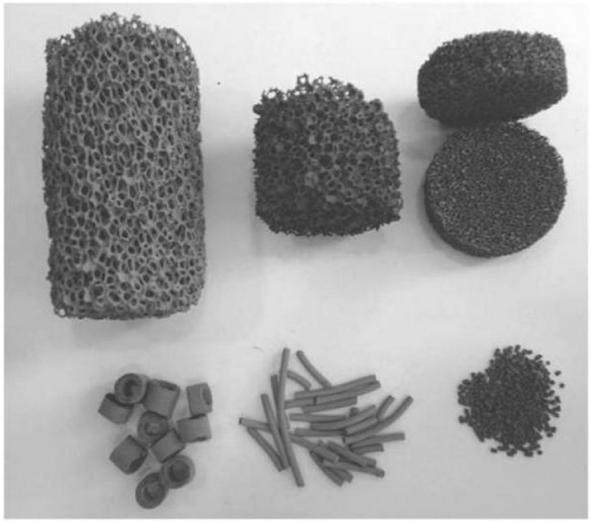

Figure 1. β-SiC with different sizes and shapes synthesized via a gas−solid reaction (LMSPC copyright).

2.2. Catalyst Preparation. TiO_2-decorated SiC-containing cobalt catalysts were prepared by pore volume impregnation of the support with cobalt nitrate (Arcros) solution (ethanol/water of 50:50, v:v %). The cobalt loading was kept at 10 wt % of the silicon carbide support, which is the lower range of cobalt loading according to the literature and patent surveys.[12,40] After impregnation, the solid was allowed to dry at room temperature for 4 h and further oven-dried at 110 °C for 8 h and calcined at 350 °C (1 °C min^{-1}) for 2 h to obtain the Co_3O_4/TiO_2−SiC catalyst precursor. The oxide form was then reduced in hydrogen (30 mL min^{-1} $g_{catalyst}^{-1}$) at 300 °C for 6 h, the obtained catalyst marked $10Co/TiO_2$−SiC. The high-porosity undecorated silicon carbide-supported cobalt catalyst, noted as 10Co/SiC, was prepared usnig the same process.

2.3. Characterization Techniques. X-ray diffraction (XRD) measurements were carried out in a Bruker D-8 Advance diffractometer equipped with a Vantec detector. The powdered sample was packed onto a glass slide. ASTM powder diffraction files were used to identify the phase present in the sample. Crystallite sizes were calculated from line broadening using the Scherrer equation.

The specific surface area of the support and the catalyst, after reduction, were determined in a Micromeritics sorptometer. The sample was outgassed at 250 °C under vacuum for 14 h to desorb moisture and adsorbed species on its surface. The measurements were carried out using N_2 as adsorbent at liquid N_2 temperature at relative pressures between 0.06 and 0.99.

TPR was determined using a Micromeritics ASAP-2100 setup under diluted hydrogen flow (10 vol % in argon) with a heating rate of 15 °C min^{-1}. The hydrogen consumption was continuously monitored with a thermal conductivity detector (TCD). The steam formed during the reduction was trapped at −88 °C using liquid−solid mixed acetone with liquid nitrogen.

Scanning electron microscopy (SEM) analyses were carried out on a JEOL 6700F microscope working at 10 kV accelerated voltage. For examination, the solid was fixed on the sample holder by a graphite paste. Before analysis, the sample was covered by a thin layer of gold to avoid charging effects. The SEM analysis allows access to the morphology of the cobalt aggregates after reduction to correlate with the metal particle size determined by the XRD line broadening.

The sample preparation for classical TEM observations was performed according to the following process: the solid was crushed in a mortar into a very fine powder. The powder was then dispersed in ethanol by sonication over 5 min. After ultrasonication, a drop of the solution was deposited on a porous carbon copper grid supporting the gold beads used as fiducial markers, and the solvent was evaporated at room temperature before introducing of the sample holder in the microscope. For the EFTEM analyses, the energy-filtered images were recorded on Si-L_{23}, Ti-L_{23} and Co-L_{23} edges using a JEOL 2100F (FEG) TEM/STEM electron microscope operating at 200 kV and equipped with a TRIDIEM post column-imaging filter from the Gatan Company. The images were acquired using a 2048 × 2048 pixel cooled CCD detector and then hardware-binned to 512 × 512 pixels with a pixel size on the order of 0.56 nm.

^{59}Co zero-field NMR experiments were performed in a homemade zero magnetic field spectrometer. The integrated spin−echo intensity was recorded every 1 MHz using a coherent pulsed NMR spectrometer with phase-sensitive detection and automated frequency scanning. The NMR spectra were taken at five different values of the excitation RF field power, covering a range of more than 1 order of magnitude. Such a procedure allowed us to determine the optimum excitation field power at each frequency and to correct for the variation of the local electronic susceptibility and, thus, of the NMR enhancement factor as a function of frequency. After this, a further correction for the usual frequency dependence of the NMR signal was applied. The NMR amplitudes obtained in such a way represent the true distribution of nuclei with a given HF. A detailed description of the technique can be found in the literature.[41,42] Measurements were done at 2, 4.2, and 77 K to be able to obtain information about the size distribution of the Co particles in the samples. The analysis was performed on the tested catalyst covered with a homogeneous solid wax layer to prevent any surface oxidation of the cobalt phase during air exposure.

2.4. Fischer−Tropsch Synthesis Reaction. Fischer−Tropsch synthesis was carried out in a tubular fixed-bed stainless steel reactor (i.d. of 6 mm) with circulating silicon oil as the heating source. The reduced catalyst (5 g of catalyst, in the form of grains 150−400 μm) was deposited between quartz wool plugs in the middle of the reactor. The reactor pressure was slowly increased from 1 to 40 bar (ramping rate of 10 bar h^{-1}) under argon. The total pressure was controlled by a back-pressure regulator (MFI Ltd.). At 40 bar, the reactor temperature was raised from room temperature to the desired reaction temperature (heating rate of 2 °C min^{-1}), then the argon flow was replaced by a 50:50 v:v % mixture of synthesis gas and argon (CO/H_2 = 1:2). The catalyst was activated under a synthesis gas/argon mixture with different synthesis gas concentrations over 3 days before evaluation under pure synthesis gas atmosphere. The catalyst bed temperature was monitored with a thermocouple (Ø = 0.3 mm) inserted inside a stainless steel finger (Ø = 1 mm) passing through the catalyst bed. The products were condensed in two high-pressure traps maintained at 85 and 15 °C, respectively. The exit gas was analyzed online by both TCD and flame ionization detector with a gas chromatograph (GC Varian 3800 equipped with a DP-1 and Carbobond capillary columns).

The liquid phase and water were condensed in the traps and analyzed off-line at the end of the test. The water was removed from the organic phase by decantation of the system. A known

dx.doi.org/10.1021/cs300729p | ACS Catal. 2013, 3, 393−404

amount (100 mg) of the organic phase, liquid hydrocarbons and waxy products, was dissolved in 3 mL of dichloromethane under sonication over 30 min, then 20 mL of CS_2 was added to the solution to ensure complete dissolution of the organic phase. For analysis, 1 μL of the solution was injected in a GC apparatus equipped with a Simdist column operated at 400 °C, which allowed the detection of hydrocarbons ranging from C_9 to C_{70}.

3. RESULTS AND DISCUSSION

3.1. Physicochemical Properties of the Supports and Catalysts. The XRD patterns of the SiC, TiC-SiC, and TiO_2−SiC supports are presented in Figure 2. The calcination step at

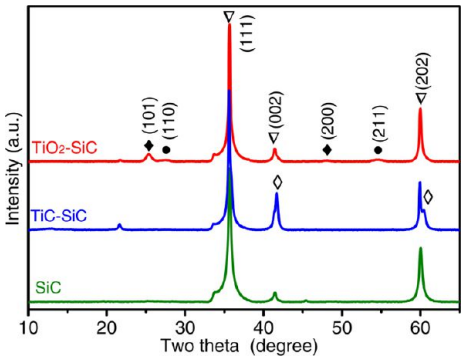

Figure 2. XRD patterns of SiC, TiC−SiC, and TiO_2−SiC supports; the TiO_2−SiC support was obtained by calcinations of the TiC−SiC at 500 °C for 2 h in air: ♦, anatase TiO_2; ●, rutile TiO_2; ▽, β-SiC; and ◊, TiC.

500 °C allows the complete transformation of the TiC into TiO_2, as confirmed by the XRD pattern, since no diffraction lines corresponding to TiC were observed.

SEM micrographs representing the morphology of titanium carbide- and titanium dioxide-decorated SiC are presented in Figure 3. The low-magnification SEM micrographs confirm the presence of macroporosity within the SiC-decorated materials before and after calcination. Medium- and high-resolution SEM micrographs evidence fragmentation of TiC particles into smaller TiO_2 particles during the calcination step.

The BET surface area, pore volume, and average pore diameter of carriers and catalysts as prepared are shown in Table 1. The introduction of TiC into the SiC matrix leads to a strong improvement of the composite specific surface area compared with the undecorated one; that is, 77 $m^2\ g^{-1}$ instead of 40 $m^2\ g^{-1}$. Such a specific surface area increase could be attributed to the formation of TiC particles evenly dispersed throughout the SiC matrix, which prevents the formation of large SiC particles with low specific surface area. According to the results, the TiC-to-TiO_2 transformation leads to a significant increase in the specific surface area of the decorated support: from 77 to 101 $m^2\ g^{-1}$. The TiO_2−SiC also contains a relatively large amount of micropores, which are expected to be generated during the calcination step to transform TiC into TiO_2. The deposition of cobalt affects two supports differently: the surface area of the undecorated SiC slightly decreases from 40 to 33 $m^2\ g^{-1}$ after deposition of 10 wt % of cobalt active phase, whereas that of the decorated SiC significantly drops from 101 to 25 $m^2\ g^{-1}$, which is mostly due to the plugging of the micropores and the formation of a new mesoporous network (Supporting Information Figure S1).

XRD was also used to characterize the crystalline structure of the catalysts. The XRD patterns of the catalysts after reduction under H_2 at 300 °C for 6 h are presented in Supporting Information Figure S2. The 10Co/SiC catalyst displays only diffraction lines corresponding to the SiC support and metallic cobalt phase without diffraction lines corresponding to the cobalt oxide phases, confirming the complete reduction of the cobalt phase. A similar reduction pattern is also observed on the decorated catalyst. The TPR results indicate that the presence of doping (i.e., TiO_2 with a loading of 17 wt %) does not alter the reduction behavior of the cobalt oxide precursor (Supporting Information Figure S2). The complete reduction of the cobalt phase was directly attributed to the low interaction between the cobalt oxide phase and the support, SiC and TiO_2, which avoids the formation of a hardly reducible cobalt phase, as usually observed with the alumina or silica supports.[22,43]

The average cobalt particle size determined by the Scherrer formula is reported in Table 1. Two methods are used to calculate the cobalt particle size. The average nanoparticle crystal size of the cobalt is ∼40−50 nm for the 10Co/SiC and

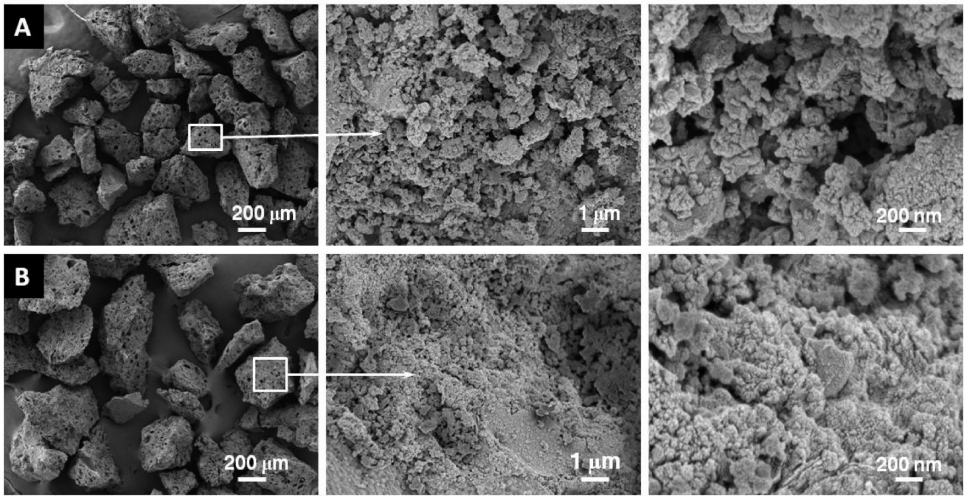

Figure 3. Representative SEM micrographs of (A) TiC−SiC and (B) TiO_2−SiC carriers. The TiC-to-TiO_2 transformation was carried out by calcination at 500 °C for 2 h in air.

dx.doi.org/10.1021/cs300729p | ACS Catal. 2013, 3, 393−404

Table 1. BET Surface Area and Pore Volume of the Undecorated and Decorated SiC Carriers and the Same after Cobalt Deposition[a]

sample	S_{BET} (m^2/g)	V_{total} (cm^3/g)	D_{BJH} (nm)	Co^0 particle size[b] (nm)	Co^0 particle size[c] (nm)	
					Co^0 fcc[d]	Co^0 hcp[e]
SiC	40	0.120	12.8			
TiO_2–SiC	101	0.123	4.4			
10Co/SiC	33	0.139	17.1	42 ± 5	51 ± 5	29 ± 5
10Co/TiO_2–SiC	25	0.082	13.0	22 ± 5	44 ± 5	14 ± 5

[a]The corresponding cobalt particle size, before and after reduction, determined by the Scherrer formula is also presented. [b]$d(Co^0) = 0.75 \times d(Co_3O_4)$. [c]$d(Co^0) = k{\cdot}\lambda/(\tau \cos \theta)$, The sample was reduced by H_2 at 300 °C for 6 h. [d]Face centered cubic (fcc) diffraction plane (111) of Co^0 particles. [e]Hexagonal close-packed (hcp) diffraction plane (101) of Co^0 particles.

~15–25 nm for the 10Co/TiO_2–SiC, the later being predicted to be the most active particle size for the FTS process.[16] The results indicate that introduction of the TiO_2 phase into the SiC matrix significantly decreases the particle size of cobalt, probably by generating a higher chemical interaction with the metal salt precursor without modifying the reduction behavior of the sample.

3.2. Reduction Behavior of Catalysts. The TPR spectra of the 10Co/SiC and 10Co/TiO_2–SiC catalysts are presented in Figure 4. The first reduction peak for both catalysts, located

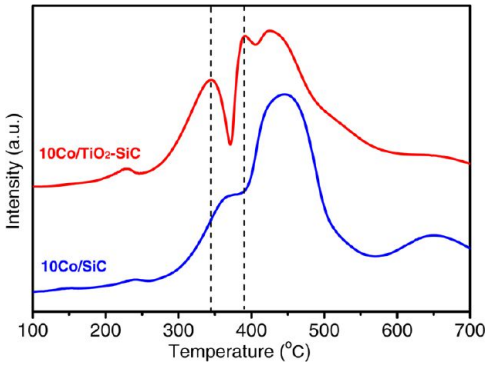

Figure 4. TPR profiles of the 10Co/SiC and 10Co/TiO_2–SiC catalysts after calcinations at 350 °C in air for 2 h.

at around 230 °C, can be attributed to the decomposition of residual cobalt nitrate in the presence of hydrogen.[14,44] In the paper published by Borg et al.,[14] calcination temperatures above 450 °C are needed to completely decompose the supported cobalt nitrate. At lower calcination temperatures, some nitrate still remains in the calcined sample, which further decomposed in the presence of hydrogen at a relatively low temperature. The reduction of cobalt oxide species started at 230 °C, and the first oxide reduction peak is typically assigned to the reduction of Co_3O_4 to CoO, although a fraction of the peak likely comprises the reduction of the larger, bulk-like CoO species to Co. The second reduction step is composed of overlapping peaks that are due to the reduction of CoO to Co. These peaks also include the reduction of cobalt species that interact with the support.[25,27,28,45] The tailing was observed after 500 °C in the TPR profile of 10Co/TiO_2–SiC, which is likely attributed to small cobalt in strong interaction with TiO_2 and the reduction of cobalt silicate- and titanate-like species.[46] The reduction of cobalt silicate-like species was observed after 550 °C on 10Co/SiC catalyst.[27,28]

The sequential TPR analysis of 10Co/TiO_2–SiC catalyst is also performed, that is, isothermal reduction at 300 °C for 2, 3, 4, and 6 h, followed by a second in situ TPR (Supporting Information Figure S3), to ensure the complete reduction of the catalyst under the applied reduction conditions. According to the results, one can state that after the reduction at 300 °C for 6 h, all the cobalt oxide was reduced, and no reduction peaks between 200–600 °C were observed in the TPR spectrum of the reduced catalyst. The reduction peaks located at around 700 °C in sequential TPR profiles (Supporting Information Figure S3) can be ascribed to the reduction of either cobalt titanate/silicate from the reaction between cobalt and the titania–silica layer or the fraction of cobalt in the inner cavities of the TiO_2–SiC support.[28,46] This peak is absent in the TiO_2–SiC support, which could again confirm the hypothesis above (Supporting Information Figure S3). Note that TPR experiments were conducted in 10% H_2/Ar mixtures, whereas the catalysts were reduced in pure hydrogen for catalytic measurements, which implies a much higher reduction rate. Chernavskii[47] reported that the hydrogen partial pressure can significantly affect the extent of the cobalt reduction. A lower reduction temperature of cobalt is usually obtained in pure hydrogen. The TPR experiment was carried out under diluted hydrogen, which could considerably lower the extent of the cobalt reduction compared with the reduction conducted under pure hydrogen flow. During the transfer, one should expect that some superficial oxidation could occur, leading to the formation of a core–shell CoO–Co phase (see TEM analysis below). Such a surface oxide layer will be rapidly reduced by the CO and H_2 mixture during the FTS process.[26,45,47]

3.3. Morphological and Microstructural Characteristics of 10Co/SiC and 10Co/TiO_2–SiC Catalysts. The corresponding SEM micrographs of the two catalysts after reduction are presented in Supporting Information Figure S4 and reveal the presence of a smaller average cobalt particle size in the decorated catalyst. The cobalt particle size is more homogeneous on the TiO_2-decorated SiC catalyst in comparison with the SiC catalyst. The cobalt particle size on the pure and TiO_2-decorated SiC catalysts was evaluated by TEM; the results are presented in Figure 5. The TEM micrographs of the 10Co/SiC catalyst indicate the presence of a relatively homogeneous cobalt particle size with an average size of around 40 nm (Figure 5A and B) dispersed throughout the support surface. The 10Co/TiO_2–SiC catalyst shows (Figure 5C and D) two difference sizes particle on catalysts surface.

To get more insight about the influence of the doping on the cobalt dispersion, high-resolution TEM analysis and 2D EFTEM were carried out. The results are presented in Figures 6 and 7. The HR-TEM analysis was carried out on several areas within a large grain of catalyst (Figure 6A). TEM micrographs of the cobalt particles localized on or next to the TiO_2 phase clearly evidence the formation of cobalt metal nanoparticles

dx.doi.org/10.1021/cs300729p | ACS Catal. 2013, 3, 393–404

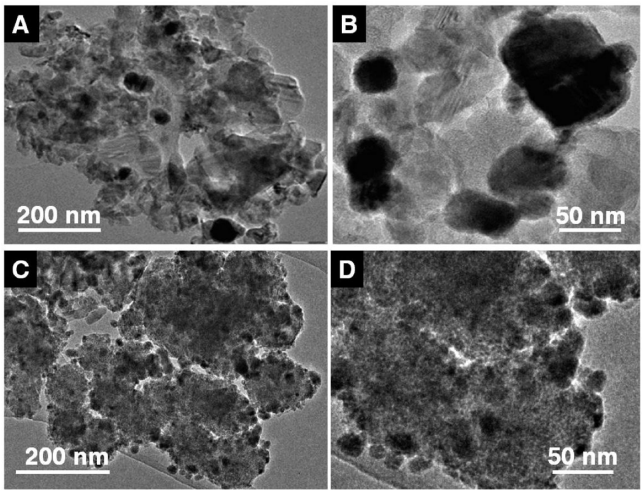

Figure 5. TEM images of (A, B) 10Co/SiC and (C, D) 10Co/TiO_2−SiC after reduction under H_2 at 300 °C for 6 h.

with size smaller than 10 nm and well separated from each other due to the relatively high metal−support interaction with the TiO_2 phase underneath (Figure 6B). Similar results have also been reported by Park et al.[48] on the cobalt-supported alumina support decorated with titanium dioxide. The suppression of the cobalt aggregation during the thermal treatment step has been attributed by the authors to the presence of a local mixed phase containing both titanium and alumina, which presents a medium metal−support interaction. It is expected that a similar phase could also be formed in the present work, which provides a highly stable anchorage surface for the cobalt particles. High-resolution TEM micrographs (Figure 6C and D) clearly evidence that the cobalt particles were highly faceted and disordered, which could provide anchorage sites for the adsorption and catalytic transformation of the carbon monoxide.

From a 2D EFTEM analysis based on electron energy loss spectroscopy (EELS) (Figure 7), one can observe that the cobalt particle size becomes smaller in contact with the TiO_2 phase. As can be seen in Figure 7, the size of the cobalt particles was significantly changed, depending on which surface they were in contact with: 5−15 nm for the Co particles in contact with TiO_2 surface and 30−50 nm for Co particles directly supported on the SiC surface. Such results again confirm the high dispersion of the cobalt particles on the TiO_2 phase, which will play a crucial role in the improvement of the FTS performance.

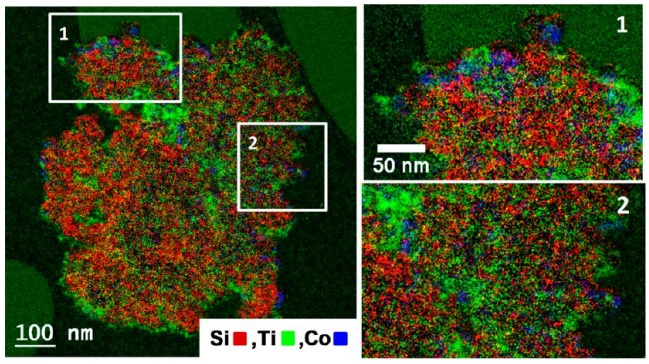

Figure 7. Representative 2D elemental relative maps deduced by EFTEM analysis for the 10Co/TiO_2−SiC sample: Ti (green), Si (red), Co (blue). The catalyst was calcined at 350 °C for 2 h, followed by a reduction under H_2 at 300 °C for 6 h.

The formation of small cobalt particles when TiO_2 was introduced to the SiC support was also confirmed by ^{59}Co solid state NMR.[25,41,42] The real advantage of this technique is that it is a bulk technique that allows one to have a general view of the cobalt phase inside the catalyst, which is not the case for the TEM or EFTEM techniques, for which only a small part of the active phase was analyzed. First of all, it has to be noted that the shape of the NMR spectra of the two samples under investigation is very similar. This shows that in contrast to the results reported in ref 25, the difference in activity of the samples was not linked to the Co structure or chemical environment but, rather, to the difference among particle size distributions. From the NMR data, we have determined the fraction of cobalt atoms for different blocking temperature

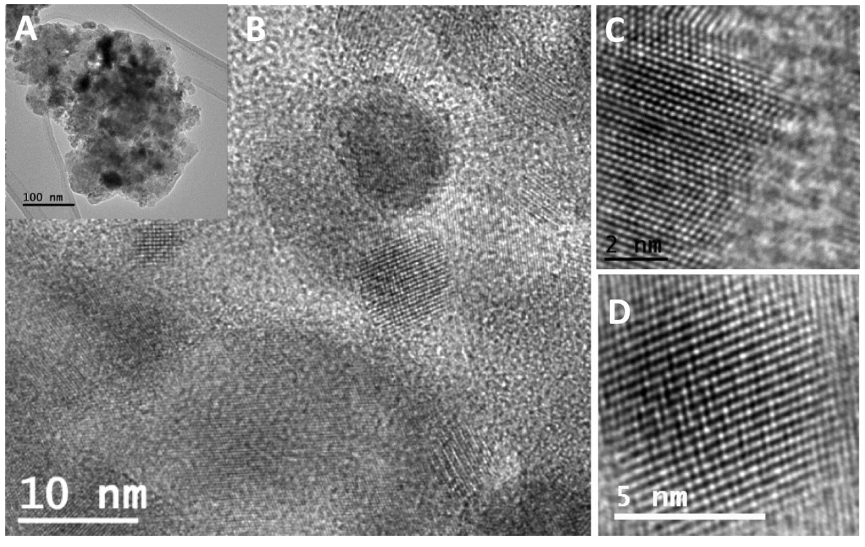

Figure 6. TEM analysis of the reduced 10Co/TiO_2−SiC catalyst. (A) Low-magnification TEM analysis. (B) Medium-resolution TEM micrograph showing the presence of several small cobalt particles next to the TiO_2 phase. (C, D) High-resolution TEM micrographs of the faceted cobalt particles.

dx.doi.org/10.1021/cs300729p | ACS Catal. 2013, 3, 393−404

ranges, presented in Figure 8A. The blocking temperature ranges correspond to Co particles size ranges. Actually the larger the blocking temperature, the larger the particle size: 4−6 nm for blocking temperature from 2 to 4.2 K; 6−15 nm for 4.2−77 K, and more than 15 nm for blocking temperature above 77 K. The technical details of the calculations can be found in the Supporting Information (Section S1).

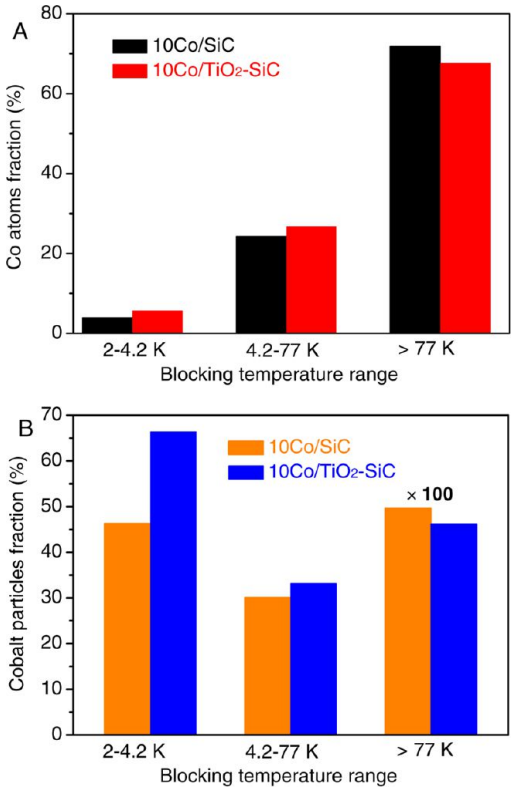

Figure 8. ^{59}Co zero field NMR results. (A) The fraction of cobalt atoms engaged in the different cobalt particle sizes as a function of the blocking temperature. (B) The relative number of cobalt particles as a function of the blocking temperature: 4−6 nm for 2−4.2 K, 6−15 nm for 4.2−77 K, and >15 nm for >77 K (note that the Co fraction is multiplied by 100 in this range for the sake of clarity).

According to the results, one can state that the fraction of cobalt atoms engaged in the small and medium cobalt particles (⌀ ranged between 4 and 15 nm) is higher on the 10Co/TiO_2−SiC than on the 10Co/SiC catalyst; however, the activity is instead related to the distribution of Co particle size rather than to the distribution of the Co atoms. From the distribution of Co atoms, assuming an average particle size in each blocking temperature range, we worked out the particle size distribution in the sample (see Supporting Information Figure S7). The result in Figure 8B shows that the doping of the SiC support by TiO_2 significantly increases the amount of the small and medium cobalt particles via a strong metal−support interaction between the deposited cobalt precursor and the TiO_2 surface in the catalyst, which in turn leads to a higher FT performance (see below). This analysis also shows that there are a large number of Co atoms (about 70%) that are clustered into very few (less that 0.5%) but very large (>15 nm) Co particles. Research focusing on decreasing the number of large cobalt clusters to obtain a highly active cobalt surface also requires further investigation.

In addition, de Jong and co-workers[16,49] found that small cobalt particles (<6 nm) led to low FTS activity and high methane selectivity. Bezemer et al.[16] studied the influence of the size of the cobalt particles on the FTS reaction using carbon nanofibers as support. The highest CoTY (19.2×10^{-5} mol_{CO} g_{Co}^{-1} s^{-1}) was observed with cobalt particle size centered at ∼8 nm under severe reaction conditions (35 bar and 250 °C). In this work, most of the cobalt atoms (>94%, Figure 8A) resulted in particles larger than 6 nm and which provide active sites with high FTS activity. Similar results have also been reported previously on SiC foam coated with a thin layer of alumina.[24] Indeed, the introduction of a thin alumina layer led to higher cobalt dispersion and an improvement in the FTS performance of the catalyst.[24]

Reuel and Bartholomew[50] have reported that the FTS activity strongly depends on the nature of the support

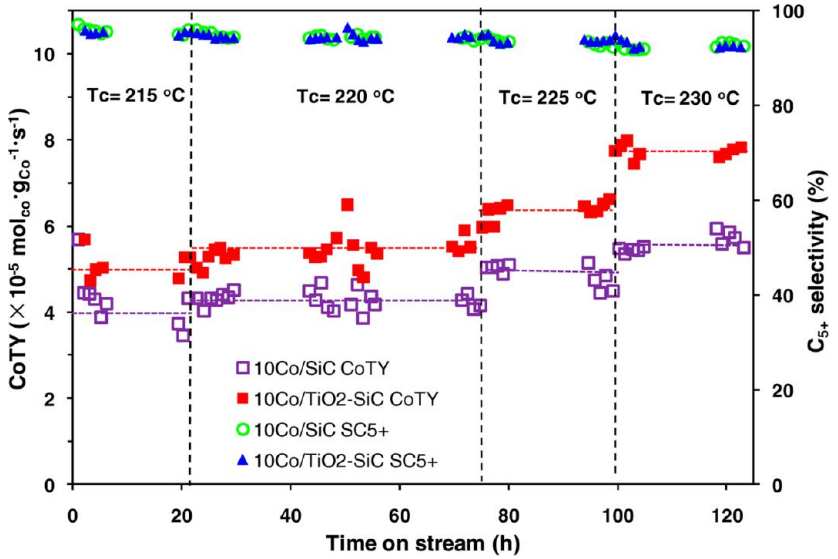

Figure 9. FTS rate and C_{5+} selectivity of the 10Co/SiC and 10Co/TiO_2−SiC catalyst as a function of the reaction temperature. Reaction conditions: H_2/CO molar ratio = 2, pure syngas, total pressure = 40 bar, GHSV (STP) = 2850 h^{-1}. The catalysts tested have already been evaluated in the FTS reaction at 215 °C and under a GHSV of 1900 h^{-1} over ∼100 h on-stream (not reported).

dx.doi.org/10.1021/cs300729p | ACS Catal. 2013, 3, 393−404

according to the following activity sequence: Co/TiO_2 > Co/Al_2O_3 > Co/SiO_2 > 100% Co > Co/MgO. However, it is worth noting that the metal−support interaction between the cobalt oxide and the TiO_2 phase was not too strong because of the relatively low reduction temperature used in the present work, which allows facile reduction of the cobalt phase according to the XRD and TPR experiments presented above. It is well-known that metal particles deposited on a TiO_2 surface exhibited higher dispersion due to the strong metal−support interaction (SMSI) when reduction was conducted at temperatures higher than 300 °C.[51] The local mixed phase formed between the TiO_2 and the surface SiO_2 on the SiC support could be responsible in part for the high dispersion of the cobalt particles, as well.

3.4. Fischer−Tropsch Synthesis (FTS) Catalytic Performance. The FTS conversion rate (expressed in terms of cobalt time yield, $mol_{CO}\ g_{Co}^{-1}\ s^{-1}$) and C_{5+} selectivity obtained on the 10Co/SiC and 10Co/TiO_2−SiC catalysts as a function of the reaction temperature and under a relatively high GHSV, 2850 h^{-1} (STP), are presented in Figure 9; the results are summarized in Table 2. The FTS rate steadily increases on both

Table 2. The Fischer−Tropsch Results Obtained on the Undecorated and Decorated SiC-Containing Cobalt Catalysts[a]

			product selectivity (%)				
catalyst	T (°C)	CO conversion (%)	CO_2	CH_4	C_2−C_4	C_{5+}	CoTY[b] ($10^{-5}\ mol_{CO}\ g_{Co}^{-1}\ s^{-1}$)
10Co/SiC	215	26.9	0	2.9	1.6	95.5	4.0
	220	28.8	0	3.7	2.0	94.3	4.3
	225	32.3	0	4.5	2.4	93.1	4.8
	230	35.4	0.1	5.4	2.9	91.6	5.3
10Co/TiO_2−SiC	215	33.9	0	3.2	1.5	95.3	5.0
	220	37.0	0	3.9	1.7	94.4	5.5
	225	43.4	0	4.5	1.9	93.6	6.5
	230	50.5	0.2	5.9	2.2	91.7	7.5

[a]Reaction conditions: GHSV (STP) = 2850 h^{-1}, H_2/CO molar ratio = 2, pure syngas, total pressure = 40 bar. [b]Cobalt-time-yield (CoTY, molar CO conversion rate per gram atom Co per hour).

catalysts with increasing reaction temperatures, whereas $S_{C_{5+}}$ selectivity remains relatively high at around 91% on both catalysts. It is worth noting that the FTS rate on the 10Co/TiO_2−SiC remains higher than the one obtained on the 10Co/SiC catalyst and steadily increases with increasing reaction temperatures. The high FTS catalytic performance of the decorated-SiC catalyst could be attributed to the better dispersion of the cobalt particles in the presence of the TiO_2 phase according to the XRD and EFTEM analysis. The FTS activity is linked to the active phase dispersion, and thus, the smaller the active phase particle size is (down to a certain level), the higher the FTS activity is.

On the undecorated SiC-based catalyst, the relatively low cobalt dispersion (40−50 nm) was linked to the lower FTS activity observed. In the decorated catalyst, the small cobalt particle size associated with the TiO_2 phase (5−15 nm) seems to be responsible for the FTS activity enhancement. The relative percent of the small cobalt particles between the decorated and undecorated catalysts, calculated by the ^{59}Co NMR method, was about 30% and correlates well with the 30% FTS conversion rate improvement between the two catalysts (Table 2). Karaca et al.[52] reported that CoPt/Al_2O_3−N1 catalyst has much higher cobalt−time yields, $8.4 \times 10^{-5}\ mol_{CO}\ g_{Co}^{-1}\ s^{-1}$, which could be attributed to higher reducibility of the smaller cobalt particles and higher concentration of cobalt active sites. The FTS activity also remains stable for the whole test, >200 h, indicating that deactivation (carbonaceous deposition, sintering, or superficial oxidation) is extremely low on such catalysts after stabilization. Similar results have already been reported by several research groups in the literature.[35,43]

The final carbon balance calculated from different experiments is 90 ± 4 wt % (Table 2). The discrepancy between the experimental and theoretical carbon balance could be due to several facts: (i) the uncertainty on the CO flow rate before and after reaction, which leads to a carbon error of 5 ± 2 wt % in the carbon balance, and (ii) the waxes that were lost during the recovery of waxes from the different traps, accounting for about 5 ± 2 wt %. The most remarkable fact is that the $S_{C_{5+}}$ selectivity remains high whatever the reaction temperature up to 230 °C. The high $S_{C_{5+}}$ selectivity obtained in the present work could be attributed to several possibilities: (i) First, the homogeneous catalyst bed temperature, thanks to the good thermal conductivity of the support and the liquid hydrocarbon film formed on the catalyst surface.[53] (ii) Second, the increased partial pressure of steam within the catalyst bed due to the relatively low space velocity.[54,55] The promoting effect of steam on the $S_{C_{5+}}$ has been proposed to be due to its inhibition of hydrogenation reactions, leading to a lower methane selectivity.[56] (iii) The meso- and macroporosity of the support, which favor the evacuation of the products and a better accessibility to the reactants. A recent work published by Holmen and co-workers[14] on the low surface area α-Al_2O_3 catalyst has also pointed out the strong influence of the support porosity on the C_{5+} selectivity. Similar high C_{5+} selectivity was also reported recently by de la Osa et al.[26,27] on the large-pore SiC-based catalysts, either undecorated or decorated with calcium. The strong influence of the support porosity on the $S_{C_{5+}}$ selectivity could be explained by the enhanced evacuation of liquid hydrocarbons from the pores of the catalyst, which significantly reduces the concentration gradients for CO versus H_2 as a result of the higher diffusivity of the later, next to the active sites localized within the pore. Indeed, a high local concentration of H_2 versus CO next to the active site leads to higher selectivity toward formation of light products by rapid hydrogenation of the intermediate olefins.

The high reaction temperature contributes to higher cobalt time yields of both catalysts in this work; however, most catalysts with relatively high activity in the literature significantly result in more rapid deactivation.[57,58] It is interesting to see that the 10Co/SiC and 10Co/TiO_2−SiC catalysts also exhibit an extremely high stability as a function of the FTS test duration according to the results presented in Figure 10. Almost no deactivation is observed on the catalyst up to 100 h on-stream, which indicates that deactivation linked with cobalt surface oxidation or sintering is unlikely to occur under the reaction conditions used in the present work.[58,59]

Furthermore, the product distribution of 10Co/SiC and 10Co/TiO_2−SiC catalysts is calculated; the results are presented in Figure 11. The chain growth factor (α) is obtained from the curve of $\ln(W_n/n)$ against n, where n is the chain length, W_n is the weight fraction of hydrocarbon with carbon numbers n. According to the results, one can state that

dx.doi.org/10.1021/cs300729p | ACS Catal. 2013, 3, 393−404

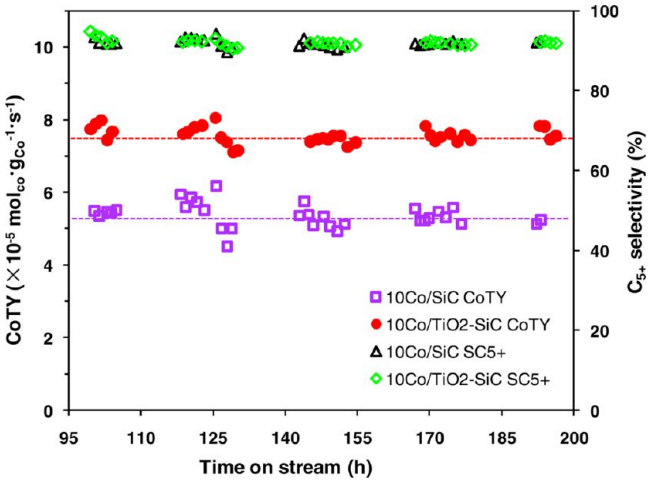

Figure 10. FTS performance and stability of the 10Co/SiC and 10Co/TiO_2−SiC catalyst as a function of time on-stream at 230 °C. Reaction conditions: H_2/CO molar ratio = 2, pure syngas, total pressure = 40 bar, GHSV (STP) = 2850 h^{-1}.

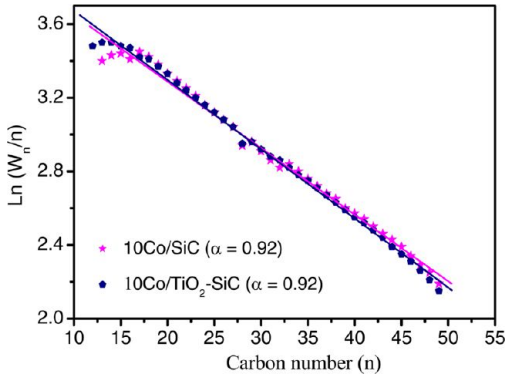

Figure 11. Calculated chain growth factor (α) from the linear portion of the liquid hydrocarbons recovered after FTS tests on the 10Co/SiC and 10Co/TiO_2−SiC catalysts.

the chain growth factor (α) is relatively high on both catalysts (0.92 for 10Co/SiC and 0.92 for TiO_2 doping catalyst), which is in good agreement with the relatively high C_{5+} selectivity obtained on both catalysts. The relatively high α value observed on the SiC-based catalysts could be linked in part to the intrinsic thermal conductivity of the support, which prevents local hot spot formation, or to the inaccuracy linked to the analysis of waxes.

In Figure 12, the FTS performances of the Ti-decorated SiC-based catalyst are compared with those reported on a similar catalyst supported on different supports.[28,48,60−62] These results clearly demonstrate that the cobalt time yield of the 10Co/TiO_2−SiC catalyst measured at 230 °C and GHSV of 2850 h^{-1} is 7.5 × 10^{-5} mol_{CO} g_{Co}^{-1} s^{-1} with a C_{5+} selectivity of 91.7%, which are typical for high catalytic activity without losing selectivity of long chain hydrocarbons.[25,28] de la Osa et al.[28] investigated the influence of the calcium as promoter on the cobalt-supported SiC catalyst and have observed a relatively high C_{5+} selectivity with high CO conversion on the 12Co−2Ca/SiC catalyst at 250 °C. The high $S_{C_{5+}}$ could be explained by the relatively high space velocity used by de la Osa et al.[28] during the FTS reaction. The small porous network support γ-Al_2O_3 replaced by the one with a larger pore size for the α-Al_2O_3-based catalyst to increase C_{5+} selectivity was investigated

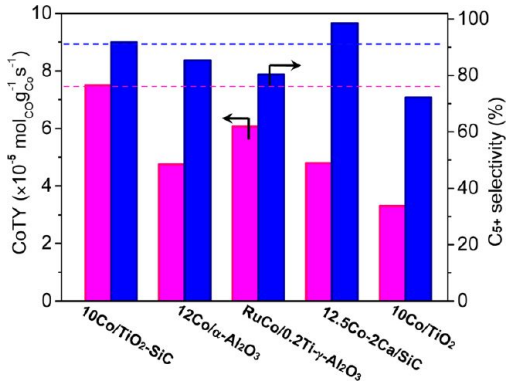

Figure 12. Comparison of FTS catalytic performance over different catalysts reported in the literature.

by Holmen and co-workers.[60,63] The large-pore α-Al_2O_3 support significantly reduces the problem of diffusion ofreactants, allowing the maintaining of a balance between CO and H_2, which leads to a high selectivity toward liquid hydrocarbons. Jalama et al.[61] used pure TiO_2 as the support and even reduced the 10Co/TiO_2 catalyst with synthesis gas instead of pure H_2 during the FTS reaction. When the catalyst was activated under synthesis gas at 350 °C, the highest FTS activity of 3.3 × 10^{-5} mol_{CO} g_{Co}^{-1} s^{-1} was obtained, as compared with 1.5 × 10^{-5} mol_{CO} g_{Co}^{-1} s^{-1} for the catalyst activated under pure hydrogen. The methane selectivity and C_{5+} selectivity were 17% and 72%, respectively. Breejen et al.[62] introduced MnO on Co/Pt/SiO_2 catalyst, followed by a calcination step in a flow of 1 vol % NO/He. For the Co/Mn/Pt/SiO_2 catalyst with an optimum Mn/Co atomic ratio of 0.08, an increase in C_{5+} selectivity from 32 (unpromoted) to 54 wt % (promoted with Mn) was found, without a significant loss in cobalt time yield, that is, 4.6 × 10^{-5} compared with 4.9 × 10^{-5} mol_{CO} g_{Co}^{-1} s^{-1}.

3.5. Influence of the Cobalt Weight Loading. In the industrial process, the metal loading is generally high at around 30 wt % to ensure the highest CO conversion per pass and to avoid costly recycling of the unreacted products. To study in depth the FTS performance of the TiO_2−SiC support, 30 wt % cobalt loading is introduced to obtain higher hydrocarbon productions per weight of catalyst.[40,64] Increasing the active phase loading per unit weight of catalyst inevitably decreases the CoTY value, and thus, comparison of the FTS performance between both cobalt-based catalysts with different cobalt loadings is carried out using a specific activity, FTS reaction rate representing the weight of long chain hydrocarbons (C_{5+}) formed per gram of catalyst per hour [$g_{C_{5+}}$ $g_{catalyst}^{-1}$ h^{-1}], instead of the cobalt time yield value, as before. Figure 13 illustrates the influence of temperature (215 and 220 °C) on the catalytic performance of 10 wt % and 30 wt % cobalt on TiO_2−SiC catalysts. On the highly cobalt-loaded catalyst (Supporting Information Table S1), the FTS activity approaches a specific rate of 0.47 $g_{C_{5+}}$ $g_{catalyst}^{-1}$ h^{-1} with a C_{5+} selectivity of 92.5%.

The stability of the Co/TiO_2−SiC catalyst is also evaluated with time on stream under more severe FTS reaction conditions on cobalt-based catalysts (i.e., space velocity of 3800 h^{-1} and reaction temperature of 230 °C) and compared with the one obtained on an undecorated SiC containing a cobalt phase promoted with 0.1 wt % of ruthenium (Figure 14 and Supporting Information Table S2).[25] According to the

dx.doi.org/10.1021/cs300729p | ACS Catal. 2013, 3, 393−404

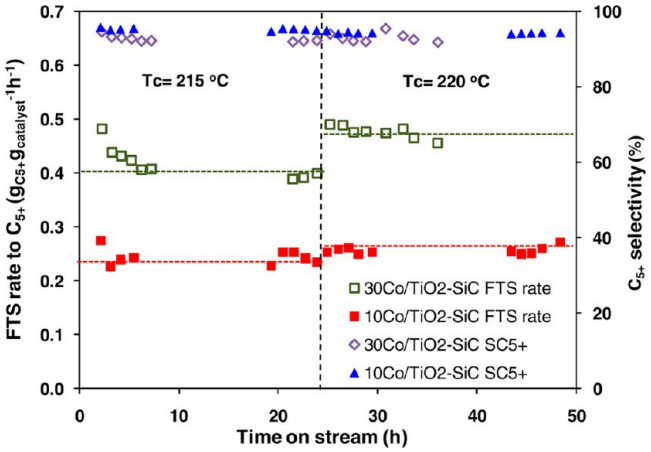

Figure 13. FTS reaction rate and C_{5+} selectivity as functions of time on-stream on $10Co/TiO_2$−SiC and $30Co/TiO_2$−SiC catalysts. Reaction conditions: H_2/CO molar ratio = 2, pure syngas, total pressure = 40 bar, GHSV (STP) = 2850 h^{-1}.

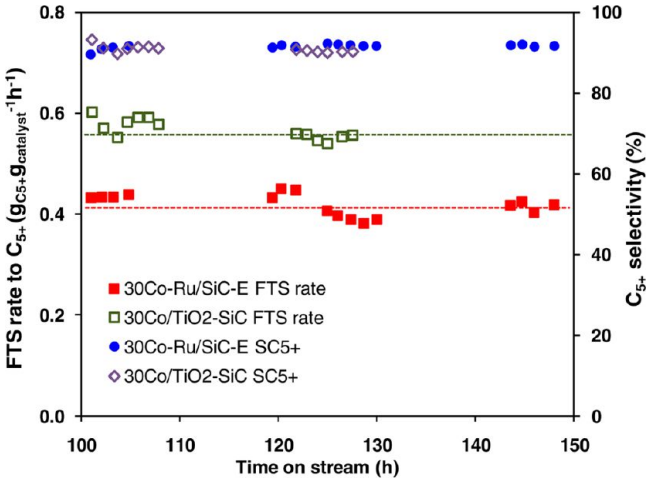

Figure 14. FTS reaction rate and C_{5+} selectivity as functions of time on-stream on $30Co/TiO_2$−SiC and Co−Ru/SiC-E[25] catalysts. Reaction conditions: H_2/CO molar ratio = 2, pure syngas, total pressure = 40 bar, GHSV (STP) = 3800 h^{-1}, reaction temperature = 230 °C.

results, the TiO_2-decorated SiC-based catalyst exhibits a higher FTS performance than the undecorated one promoted with a noble metal. The FTS activity also remains stable for about 30 h on stream and confirms the relatively high stability of the catalyst promoted with TiO_2. The specific rate steadily increased to 0.56 $g_{C_{5+}}$ $g_{catalyst}^{-1}$ h^{-1} with a relatively higher C_{5+} selectivity, 90.6%. On the bais of our knowledge, the current result is the best among all the noble metal, promoter-free, cobalt-based catalysts in the literature, with both the highest specific rate and long-chain hydrocarbon selectivity. It is also worth noting that the specific rate obtained on the unpromoted $30Co/TiO_2$−SiC catalyst is relatively high and more stable compared with those promoted by noble metal obtained on the $Co-Re/Al_2O_3$, $Co-Re/SiO_2$, and $Co-Re/TiO_2$ catalysts, as reported by Tsakoumis et al.[58] The most active catalyst reported in the work of Tsakoumis et al.[58] is the $Co-Re/Al_2O_3$, with an initial reaction rate of about 0.56 g_{CH_2} $g_{catalyst}^{-1}$ h^{-1}, followed by a rapid deactivation down to 0.45 g_{CH_2} $g_{catalyst}^{-1}$ h^{-1} after about 22 h on-stream. It is also worth mentioning that the $30Co/TiO_2$−SiC catalyst has been run for more than 200 h under different reaction conditions.

4. CONCLUSIONS

Silicon carbide decorated with TiO_2 can be efficiently employed as a support for the cobalt phase in the low-temperature fixed-bed Fischer−Tropsch synthesis (FTS) reaction. The adequate pore size distribution of the support (i.e. meso- and macropore contribution) also facilitates the evacuation of the intermediate products, keeping the active sites more available for reactants. The intermediate product evacuation thus reduces the gradient concentration of the H_2 and CO next to the active site and prevents the formation of light products while keeping the liquid hydrocarbon selectivity in a high range, even at a high conversion rate. The meso- and macroporosity of the support also prevent deactivation of the catalyst by pore plugging due to the formation of carbonaceous residues.

This study underlines once again the benefit of the EFTEM technique analytical mode for providing one-to-one correspondence between the morphology and chemical composition on a three-dimensional surface at the nanoscale. In particular and for the first time, it allows showing that the medium metal−support interaction between the cobalt nanoparticles and TiO_2 leads to the formation of small cobalt particles with enhanced FTS activity compared with the same catalyst supported on the undecorated SiC support. The presence of a higher amount of small and medium cobalt particles on the TiO_2-decorated SiC catalyst compared with what was observed on the undecorated one was also confirmed by ^{59}Co NMR. Indeed, such small metal particles (<15 nm) with a large fraction of surface atoms significantly contribute to the enhancement of the conversion rate of reactants into products. After titanium doping, the cobalt time yield increased from 5.3×10^{-5} to 7.5×10^{-5} mol_{CO} g_{Co}^{-1} s^{-1} at 230 °C, while the C_{5+} selectivity is maintained in the same level: 91.7% and 91.6%, respectively. It is interesting to note that TiO_2−SiC-supported catalysts exhibit a relatively high specific rate along with a high liquid hydrocarbon selectivity compared with those previously reported in the literature under differential conditions. It can also be noted that the NMR analyses revealed that a large fraction of Co atoms (about 70%) are included in a small number of very large particles that most probably are not very efficient for the FTS process. This allows us to think that it is still possible to strongly improve the efficiency of this kind of catalyst.

Finally, the high metal loading of 30 wt % cobalt is similar to those of commercial FTS catalysts and avoids costly recycling of the unreacted products. The superior FT specific rate of 0.56 $g_{C_{5+}}$ $g_{catalyst}^{-1}$ h^{-1} with C_{5+} selectivity still at 91% was observed along the whole test. Work is ongoing to evaluate the influence of the support morphology on the Fischer−Tropsch performance on such a catalyst.

■ ASSOCIATED CONTENT

Supporting Information

Pore size distribution of TiO_2−SiC support and its reduced catalyst, XRD and SEM of reduced catalysts, sequential TPR of $10Co/TiO_2$−SiC catalyst and Co zero-field NMR (Figures S1−S5 and Section S1). Fischer−Tropsch results of different cobalt loading catalysts (Tables S1 and S2). This material is available free of charge via the Internet at http://pubs.acs.org.

dx.doi.org/10.1021/cs300729p | ACS Catal. 2013, 3, 393−404

AUTHOR INFORMATION

Corresponding Author

*E-mail: yue-feng.liu@etu.unistra.fr (Y.L.), cuong.pham-huu@unistra.fr (C.P.-H.).

Notes

The authors declare no competing financial interest.

ACKNOWLEDGMENTS

The present project was financially supported by TOTAL S.A. and Sicat Co. Y.L. thanks the China Scholarship Council (CSC) for a grant during his Ph.D. stay at the LMSPC. B.d.T. thanks TOTAL S.A. for financial support during his Ph.D. at the LMSPC. The SEM, ^{59}Co NMR, and EFTEM analysis experiments were carried out at the facilities of IPCMS (UMR 7504 du CNRS). Dominique Begin, Thierry Romero, and Jingjie Luo (LMSPC) are gratefully acknowledged for discussions and experimental assistance.

REFERENCES

(1) Khodakov, A. Y.; Chu, W.; Fongarland, P. *Chem. Rev.* **2007**, *107*, 1692.
(2) Dry, M. E. *Catal. Today* **2002**, *71*, 227.
(3) Khodakov, A. Y. *Catal. Today* **2009**, *144*, 251.
(4) Leckel, D. *Energy Fuels* **2009**, *23*, 2342.
(5) Zhang, Q. H.; Kang, J. C.; Wang, Y. *ChemCatChem* **2010**, *2*, 1030.
(6) Whitesides, G. M.; Crabtree, G. W. *Science* **2007**, *315*, 796.
(7) Eggenhuisen, T. M.; den Breejen, J. P.; Verdoes, D.; de Jongh, P. E.; de Jong, K. P. *J. Am. Chem. Soc.* **2010**, *132*, 18318.
(8) Perego, C.; Bortolo, R.; Zennaro, R. *Catal. Today* **2009**, *142*, 9.
(9) Yang, J. I.; Yang, J. H.; Kim, H. J.; Jung, H.; Chun, D. H.; Lee, H. T. *Fuel* **2010**, *89*, 237.
(10) Tsubaki, N.; Sun, S. L.; Fujimoto, K. *J. Catal.* **2001**, *199*, 236.
(11) Chu, W.; Wang, L. N.; Chernavskii, P. A.; Khodakov, A. Y. *Angew. Chem. Int. Ed.* **2008**, *47*, 5052.
(12) Oukaci, R.; Singleton, A. H.; Goodwin, J. G. *Appl. Catal., A* **1999**, *186*, 129.
(13) Storsaeter, S.; Borg, O.; Blekkan, E. A.; Totdal, B.; Holmen, A. *Catal. Today* **2005**, *100*, 343.
(14) Borg, O.; Dietzel, P. D. C.; Spjelkavik, A. I.; Tveten, E. Z.; Walmsley, J. C.; Diplas, S.; Eri, S.; Holmen, A.; Ryttera, E. *J. Catal.* **2008**, *259*, 161.
(15) Bezemer, G. L.; Radstake, P. B.; Koot, V.; van Dillen, A. J.; Geus, J. W.; de Jong, K. P. *J. Catal.* **2006**, *237*, 291.
(16) Bezemer, G. L.; Bitter, J. H.; Kuipers, H. P. C. E.; Oosterbeek, H.; Holewijn, J. E.; Xu, X. D.; Kapteijn, F.; van Dillen, A. J.; de Jong, K. P. *J. Am. Chem. Soc.* **2006**, *128*, 3956.
(17) Chen, W.; Fan, Z. L.; Pan, X. L.; Bao, X. H. *J. Am. Chem. Soc.* **2008**, *130*, 9414.
(18) Bezemer, G. L.; Remans, T. J.; van Bavel, A. P.; Dugulan, A. I. *J. Am. Chem. Soc.* **2010**, *132*, 8540.
(19) Zarubova, S.; Rane, S.; Yang, J.; Yu, Y. D.; Zhu, Y.; Chen, D.; Holmen, A. *ChemSusChem* **2011**, *4*, 935.
(20) Jacobs, G.; Ji, Y. Y.; Davis, B. H.; Cronauer, D.; Kropf, A. J.; Marshall, C. L. *Appl. Catal., A* **2007**, *333*, 177.
(21) Voss, A.; Borgmann, D.; Wedler, G. *J. Catal.* **2002**, *212*, 10.
(22) Jacobs, G.; Das, T. K.; Zhang, Y. Q.; Li, J. L.; Racoillet, G.; Davis, B. H. *Appl. Catal., A* **2002**, *233*, 263.
(23) Wang, Y.; Vanderwiel, D. P.; Tonkovich, A. L. Y.; Gao, Y.; Baker, E. G. Battelle Memorial Institute; U.S. Patent 7045486, 2006.
(24) Lacroix, M.; Dreibine, L.; de Tymowski, B.; Vigneron, F.; Edouard, D.; Begin, D.; Nguyen, P.; Pham, C.; Savin-Poncet, S.; Luck, F.; Ledoux, M. J.; Pharn-Huu, C. *Appl. Catal., A* **2011**, *397*, 62.
(25) de Tymowski, B.; Liu, Y. F.; Meny, C.; Lefevre, C.; Begin, D.; Nguyen, P.; Pham, C.; Edouard, D.; Luck, F.; Pham-Huu, C. *Appl. Catal., A* **2012**, *419*, 31.
(26) de la Osa, A. R.; de Lucas, A.; Romero, A.; Valverde, J. L.; Sanchez, P. *Catal. Today* **2011**, *176*, 298.
(27) de la Osa, A. R.; de Lucas, A.; Diaz-Maroto, J.; Romero, A.; Valverde, J. L.; Sanchez, P. *Catal. Today* **2012**, *187*, 173.
(28) de la Osa, A. R.; de Lucas, A.; Sanchez-Silva, L.; Diaz-Maroto, J.; Valverde, J. L. *Fuel* **2012**, *95*, 587.
(29) Galvis, H. M. T.; Bitter, J. H.; Khare, C. B.; Ruitenbeek, M.; Dugulan, A. I.; de Jong, K. P. *Science* **2012**, *335*, 835.
(30) Ledoux, M. J.; Pham-Huu, C. *CATTECH* **2001**, *5*, 226.
(31) Deneuve, A.; Florea, I.; Ersen, O.; Nguyen, P.; Pham, C.; Begin, D.; Edouard, D.; Ledoux, M. J.; Pham-Huu, C. *Appl. Catal., A* **2010**, *385*, 52.
(32) Philippe, R.; Lacroix, M.; Dreibine, L.; Pham-Huu, C.; Edouard, D.; Savin, S.; Luck, F.; Schweich, D. *Catal. Today* **2009**, *147*, S305.
(33) Martinez, A.; Prieto, G.; Rollan, J. *J. Catal.* **2009**, *263*, 292.
(34) Lesaint, C.; Glomm, W. R.; Borg, O.; Eri, S.; Rytter, E.; Oye, G. *Appl. Catal., A* **2008**, *351*, 131.
(35) Witoon, T.; Chareonpanich, M.; Limtrakul, J. *Fuel Process. Technol.* **2011**, *92*, 1498.
(36) Xiong, H. F.; Motchelaho, M. A. M.; Moyo, M.; Jewell, L. L.; Coville, N. J. *J. Catal.* **2011**, *278*, 26.
(37) Midgley, P. A.; Weyland, M. *Ultramicroscopy* **2003**, *96*, 413.
(38) Mobus, G.; Doole, R. C.; Inkson, B. J. *Ultramicroscopy* **2003**, *96*, 433.
(39) Nguyen, P.; Pham, C. *Appl. Catal., A* **2011**, *391*, 443.
(40) Diehl, F.; Khodakov, A. Y. *Oil Gas Sci. Technol.* **2009**, *64*, 11.
(41) Nuclear Magnetic Resonance in Ferromagnetic Multilayers and Nanocomposites: Investigations of Their Structural and Magnetic Properties Source: Modern Magnetic Resonance. In *Modern Magnetic Resonance*; Webb, G., Ed.; Springer: Heidelberg, Germany, 2006; pp 1493−1498.
(42) Panissod, P.; Meny, C. *Appl. Magn. Reson.* **2000**, *19*, 447.
(43) Storsaeter, S.; Totdal, B.; Walmsley, J. C.; Tanem, B. S.; Holmen, A. *J. Catal.* **2005**, *236*, 139.
(44) Borg, O.; Blekkan, E. A.; Eri, S.; Akporiaye, D.; Vigerust, B.; Rytter, E.; Holmen, A. *Top. Catal.* **2007**, *45*, 39.
(45) Tavasoli, A.; Abbaslou, R. M. M.; Dalai, A. K. *Appl. Catal., A* **2008**, *346*, 58.
(46) Riva, R.; Miessner, H.; Vitali, R.; Del Piero, G. *Appl. Catal., A* **2000**, *196*, 111.
(47) Chernavskii, P. A.; Khodakov, A. Y.; Pankina, G. V.; Girardon, J. S.; Quinet, E. *Appl. Catal., A* **2006**, *306*, 108.
(48) Park, S. J.; Kim, S. M.; Woo, M. H.; Bae, J. W.; Jun, K. W.; Ha, K. S. *Appl. Catal., A* **2012**, *419*, 148.
(49) den Breejen, J. P.; Radstake, P. B.; Bezemer, G. L.; Bitter, J. H.; Froseth, V.; Holmen, A.; de Jong, K. P. *J. Am. Chem. Soc.* **2009**, *131*, 7197.
(50) Reuel, R. C.; Bartholomew, C. H. *J. Catal.* **1984**, *85*, 78.
(51) Li, Y. Z.; Fan, Y. N.; Yang, H. P.; Xu, B. L.; Feng, L. Y.; Yang, M. F.; Chen, Y. *Chem. Phys. Lett.* **2003**, *372*, 160.
(52) Karaca, H.; Safonova, O. V.; Chambrey, S.; Fongarland, P.; Roussel, P.; Griboval-Constant, A.; Lacroix, M.; Khodakov, A. Y. *J. Catal.* **2011**, *277*, 14.
(53) Zhu, X. W.; Lu, X. J.; Liu, X. Y.; Hildebrandt, D.; Glasser, D. *Ind. Eng. Chem. Res.* **2010**, *49*, 10682.
(54) Rytter, E.; Eri, S.; Skagseth, T. H.; Schanke, D.; Bergene, E.; Myrstad, R.; Lindvag, A. *Ind. Eng. Chem. Res.* **2007**, *46*, 9032.
(55) Krishnamoorthy, S.; Tu, M.; Ojeda, M. P.; Pinna, D.; Iglesia, E. *J. Catal.* **2002**, *211*, 422.
(56) Iglesia, E. *Appl. Catal., A* **1997**, *161*, 59.
(57) Borg, O.; Hammer, N.; Eri, S.; Lindvag, O. A.; Myrstad, R.; Blekkan, E. A.; Ronning, M.; Rytter, E.; Holmen, A. *Catal. Today* **2009**, *142*, 70.
(58) Tsakoumis, N. E.; Ronning, M.; Borg, O.; Rytter, E.; Holmen, A. *Catal. Today* **2010**, *154*, 162.
(59) Yu, G. B.; Sun, B.; Pei, Y.; Xie, S. H.; Yan, S. R.; Qiao, M. H.; Fan, K. N.; Zhang, X. X.; Zong, B. N. *J. Am. Chem. Soc.* **2010**, *132*, 935.
(60) Rane, S.; Borg, O.; Yang, J.; Rytter, E.; Holmen, A. *Appl. Catal., A* **2010**, *388*, 160.

(61) Jalama, K.; Kabuba, J.; Xiong, H. F.; Jewell, L. L. *Catal. Commun.* **2012**, *17*, 154.
(62) den Breejen, J. P.; Frey, A. M.; Yang, J.; Holmen, A.; van Schooneveld, M. M.; de Groot, F. M. F.; Stephan, O.; Bitter, J. H.; de Jong, K. P. *Top. Catal.* **2011**, *54*, 768.
(63) Aaserud, C.; Hilmen, A. M.; Bergene, E.; Eric, S.; Schanke, D.; Holmen, A. *Catal. Lett.* **2004**, *94*, 171.
(64) Davis, B. H. *Ind. Eng. Chem. Res.* **2007**, *46*, 8938.

■ NOTE ADDED AFTER ASAP PUBLICATION

After this paper was published ASAP February 13, 2013, some corrections were made to the text. The corrected version was reposted February 14, 2013.